Photolithographed Whispering Gallery Mode Microdisk Cavities Coupled to Semiconductor Quantum Dots

Charlie Kersuzan, Sergei Celaj, Willy Daney de Marcillac, Thomas Pons, Agnès Maître

Photolithographied whispering gallery mode microdisk cavities coupled to semiconductor quantum dots

Charlie Kersuzan,[†,‡] Sergei Celaj,[‡] Willy Daney de Marcillac,[‡] Thomas Pons,[*,†] and Agnès Maître[*,‡]

†*Laboratoire de Physique et d'Etude des Matériaux, EPSCI-PSL Research University, CNRS, Sorbonne Université UMR8213, 10, rue Vauquelin, 75005 Paris, France*

‡*Institut des Nanosciences de Paris, CNRS, Sorbonne Université UMR7588, 4 place Jussieu, 75005 Paris, France*

E-mail: thomas.pons@espci.fr; agnes.maitre@sorbonne-universite.fr

Abstract

The development of whispering gallery mode (WGM) cavities as integrated light sources and sensors requires the scalable, low cost fabrication of high quality microcavities with integrated light sources. In particular, semiconductor quantum dots (QDs) are promising nanoemitters with highly desirable photostability and tunable optical properties, but their controlled coupling to polymeric microcavities is hampered by chemical incompatibility between the QD surface ligands and the high refractive index polymers used to fabricate microcavities. In this article, we present a new type of polymeric whispering gallery mode microdisk cavity realized by photolithography on an industrial photosensitive epoxy resin. We demonstrate the homogeneous labeling of these microcavities by CdSe/CdS/Zns QDs thanks to a novel surface ligand and the

coupling of their emission to WGMs from the microdisk cavity. The spectral properties of the WGM-coupled emission are consistent with electromagnetic simulations and indicate that the WGM quality factors can reach values higher than 6000. This demonstrates that photolithography of high refractive epoxy resins followed by integration of functionalized QDs enables the realization of well controlled, high quality WGM microresonators.

Keywords

microcavities, photolithography, whispering gallery mode, quantum dot, surface chemistry

1 Introduction

Whispering Gallery Modes (WGM) microcavities exhibit extremely interesting optical properties such as a high quality factor (Q), a strong evanescent field extending over a few hundreds of nanometers from the micro-cavity's surface and a small mode volume[1–3]. Such properties have made them intensively studied for diverse applications. Their high Q factor and small mode volumes are interesting for building microlasers and integrate them in photonic structures as a light source or a frequency filter[2,3]. Bio-detection systems and chemical sensing based on WGM microcavities and their strong, short range evanescent field has also been experimented[4–7].

The first WGM microcavities were made by melting the tip of a glass stick, which reshaped into a sphere due to surface tension effects[1], however this method allowed poor size control and only relatively large spheres[3]. Melting the end of a fiber tip with a splicer enabled the same spherical cavities with a better size control and lower minimal diameters, down to 40 µm[3]. Microbottle resonators were made from fibers as well by a heat and pull method[8]. Another type of cavity based on fibers, in-fiber cavities, designed by micromachining were also developed[9]. With these methods, high quality factor (Q) WGM as high as

10^8 were obtained, but only one cavity at a time could be made. Another method consisting of growing crystal structures such as GaN rods by molecular beam epitaxy[10] or ZnO microdisks by vapor phase transport[11]. These methods are effective at making a large number of cavities simultaneously, but require a long processing time, heavy equipment and are expensive to make. The same goes for microtoroids, which are made from silica onto a silicon substrate[12]. Another approach developed is based on polymeric microcavities. The use of polymer allows a good control of the shape and has been used in several ingenious ways. Microbottle resonators are fabricated by pouring SU8, a photosensitive epoxy resin onto a fiber[13], before cross-linking it by UV exposure. Spheres and half spheres of Araldite resin[14], or polymer fibers made of poly(methylmethacrylate)[15], could reach Q factors of 8000. PDMS micro-droplets made from a sol-gel process have also been used as microcavities[16]. A different approach consists of using the naturally formed bubbles and droplets from evaporating films, however this method does not allow control of position and size of the resonators.[17,18] A promising method to design microcavities is by using the inkjet technique, enabling fast fabrication of WGM microresonator arrays onto a substrate. However, this method is only suitable for low viscosity materials, and control of resonators size is approximative for the moment.[19–23] A photolithographic approach using polymeric material has the benefit of easy fabrication process, position and size control over the cavities and easy functionalization of the surface with different materials[6]. In particular, the photosensitive SU8 resin present several advantages such as low cost, easy processibility, low surface rugosity, excellent transparency in the visible range and high refractive index.

Once the cavity is made, light has to be injected and collected from the cavity. High quality optical modes are not coupled efficiently to far field electromagnetic radiation. Coupling microcavities with external light sources and collection systems therefore involves coupling via local evanescent field using prisms, tapered fibers, lithographied waveguides or local antennas[24]. These methods enable high coupling efficiencies but require high precision positioning and can only address a small number of cavities. Another approach is to directly

integrate fluorescent emitters inside the cavity, near the maximum of the optical mode. By doing so, the excitation of the mode can be performed externally, via excitation of the fluorescent emitters from the far field, followed by their de-excitation into the local optical mode. This option has the advantage of simplifying the system and enabling parallel addressing of a large number of microcavities. In particular, colloidal Quantum Dots (QDs) like core/shell CdSe/CdS are excellent candidates as internal light source, due to their optical properties (narrow emission spectra, high photostability and quantum yields, low lasing threshold[25]) and their solution processibility. However, inserting nanocrystals in a WGM microcavity poses challenging issues. Indeed, the nanocrystals need to be homogeneously dispersed in the polymer matrix, since the formation of clusters would lead to important scattering losses, thus drastically reducing the Q factor of the cavity. Several methods have been developed for QDs dispersion inside WGM microcavities. A first strategy is the modification of polymer surface[26–30]. However, this type of approach requires to process the polymeric cavity after its realization, which can induce roughness on the surface and greatly decrease the quality factor[29,31–34]. Another approach consists of functionalizing the polymeric material with fluorescent molecules.[35] Bahrum et al. used this approach using fluorescent dyes incorporated into a SU8 matrix. This interesting approach can be adapted to QDs to benefit from their highly interesting photoemission properties.

In this manuscript, we demonstrate a simple approach to realize controllable fabrication of high quality microcavities with internal QD light sources. We develop a simple photolithography process of SU8 to fabricate cylindrical microdisks of controllable sizes with high quality factors. We then develop a novel QD surface ligand to functionalize QDs and enable their homogeneous dispersion in SU8 composite and use them as internal light sources to excite WGMs inside these microdisks. We show that the emission of QDs couples efficiently to the WGMs of the microdisks, analyze the spectral properties of WGMs in microdisks of different sizes and compare experimental results with simulations.

2 Results and discussion

2.1 Microcavity Fabrication

In order to make low-cost, high quality and easily controllable WGM microcavities, we selected SU8 as photopolymerizable resin. SU8 is an epoxy resin which is easy to process, has a high-aspect-ratio, a low surface roughness and high refractive index (1.58 at 600nm). It is transparent in the visible spectrum, which makes it a suitable candidate as WGM microcavities in the visible range. Optical lithography by direct laser writing[36] was performed using a 405 nm continuous laser to fabricate cylindrical microdisks (Figure 1a). These cavities are expected to support WGMs in the plane perpendicular to the microdisks axis. We optimized the process in order to obtain size-controlled, smooth microdisks with straight side walls perpendicular to the cylinder axis essential to obtain high quality WGMs.

In order to isolate WGMs from the glass coverslip and prevent radiative leaking into the substrate, a thin (100 nm) gold layer was first deposited on the glass coverslips. SU8 was uniformly spread onto the gold film by spin-coating in order to obtain a thickness of around 3 µm, as measured by mechanical profilometry and confirmed by SEM imaging (Figure 1b). The resin was then soft-baked at 75°C . After laser exposure, a post exposure bake is performed at 95°C for 2 min to strengthen the resin cross-linking. Development is then performed by immersing the cover-slip in propyleneglycol methylether acetate (PGMEA) for 2 min. As development increases microcavity surface roughness, a hard bake step (110°C, 1 min) is necessary to smooth the walls of the cavity. Details of the different parameters are given in supplementary, Figures S1, S2, S3.

A typical SEM image of a microdisk after the complete process is shown in Figure 1b, showing smooth vertical walls. The height of the microdisk (1.7 µm) is slightly smaller than the thickness of the initial SU8 layer, while its diameter depends on the laser energy deposited during the photopolymerization process. In Figure 1c, we show that we can finely control the size of the cavities simply by controlling the exposure conditions. Increasing exposure time

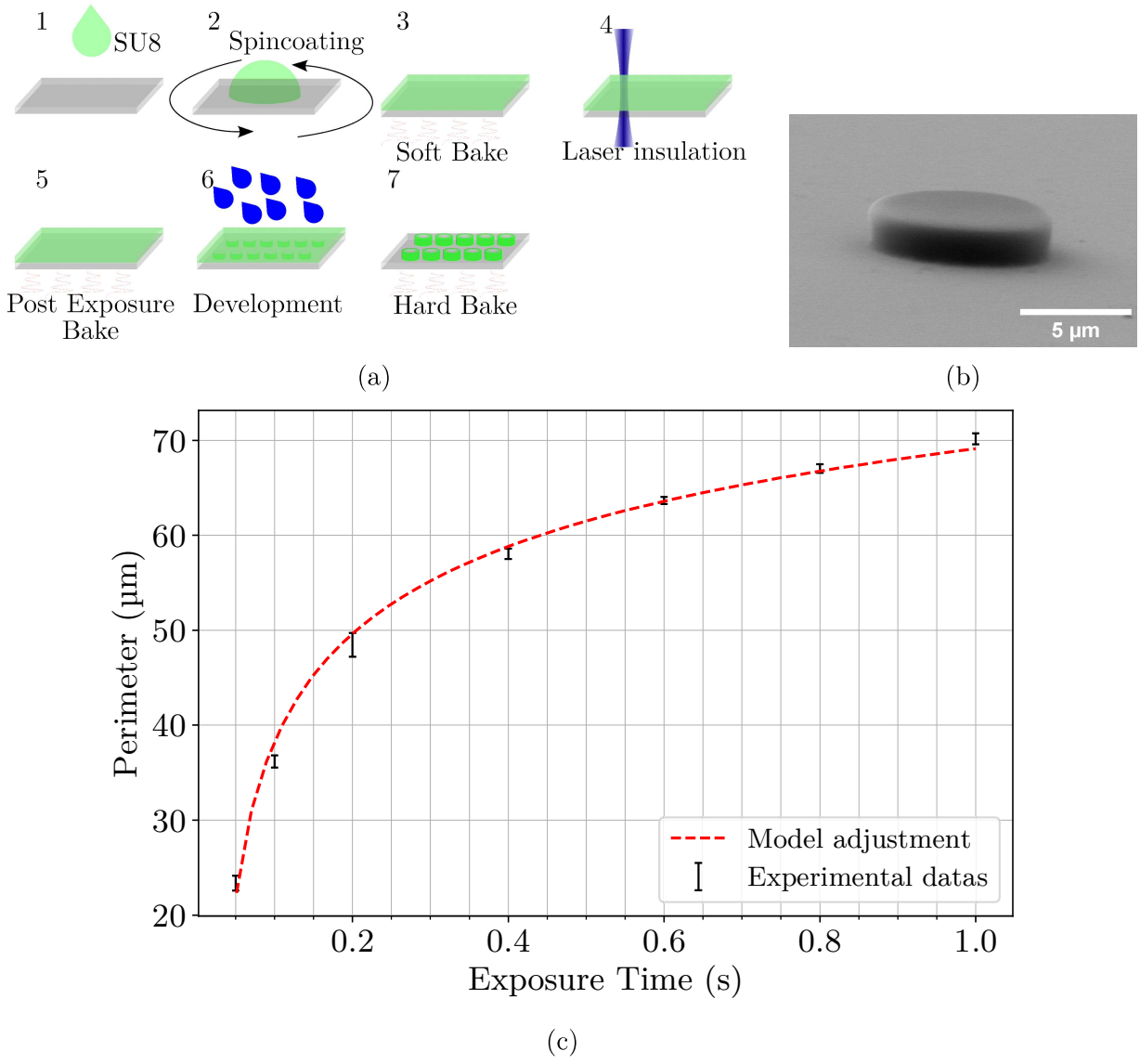

Figure 1: a) Scheme of the lithographic process: 1:dropping SU8, 2:spin-coating, 3:soft-baking, 4:laser writing, 5:post exposure bake, 6:immersion in PGMEA for development, 7:hard bake ; b) SEM image of a microdisk at the end of the fabrication process; c) Microdisk perimeter as a function of laser exposure time. CW laser power $P_0 = 700\mu W$ and laser waist $w_0 = 9.0 \pm 0.5\ \mu m$. Error bars represent the standard deviation of the microdisk perimeters for each exposure time, measured over 20 microdisks.

and/or laser intensity results in wider microdisks, with an excellent reproducibility (typically 1% standard deviation in size for each exposure condition).

Indeed, we consider that locally crosslinking the SU8 requires a minimum irradiation energy to enable sufficient polymerization and cross-linking so that the microdisk retains its morphology after development. Below this energy, the SU8 resin is not sufficiently crosslinked and dissolves in the solvent during development. Assuming a laser Gaussian beam profile with waist w_0, incident power P_0 and exposure time t, the energy deposited per unit surface as a function of the distance to the center of the beam, $W(r,t)$, is:

$$W(r,t) = 2\frac{P_0 t}{\pi w_0^2} * \exp\left(-\frac{2*r^2}{w_0^2}\right) \tag{1}$$

If W_{lim} is the minimal laser energy per unit surface necessary to cross-link the resin, the perimeter of the final microdisk, L_{disk} is going to be exactly the perimeter at which the energy per unit surface is equal to W_{lim}, and should vary as the square root of the logarithm of the exposure time:

$$L_{disk} = 2\pi w_0 * \sqrt{\frac{1}{2}\ln\left(\frac{2P_0 t}{\pi w_0^2 W_{lim}}\right)} \tag{2}$$

Figure 1c shows that this trend predicted from Eq. 2 is indeed observed, which enables to tune the perimeter between 30 µm and 70 µm simply by changing the exposure time for each microdisk. This enables the rapid realization of patterns of microdisks of different sizes on the same substrate, by successive illumination of different spots within the SU8 layer. Our model enables us to calculate the minimal energy per unit surface required to crosslink SU8 films under our conditions at 405nm, $W_{lim} = (2.21 \pm 0.07) \cdot 10^4 mJ \cdot cm^{-2}$. Moreover, our model retrieves the value of the waist of the laser beam with a value of $w_0 = 8.5 \pm 0.1 \mu m$, consistent with our experimental measurement of $w_{exp} = 9.0 \pm 0.5 \mu m$. This confirms the validity of our model allowing the prior calculation of power and exposure time required to achieve a definite microdisk size.

2.2 Quantum Dots dispersion in the microcavity

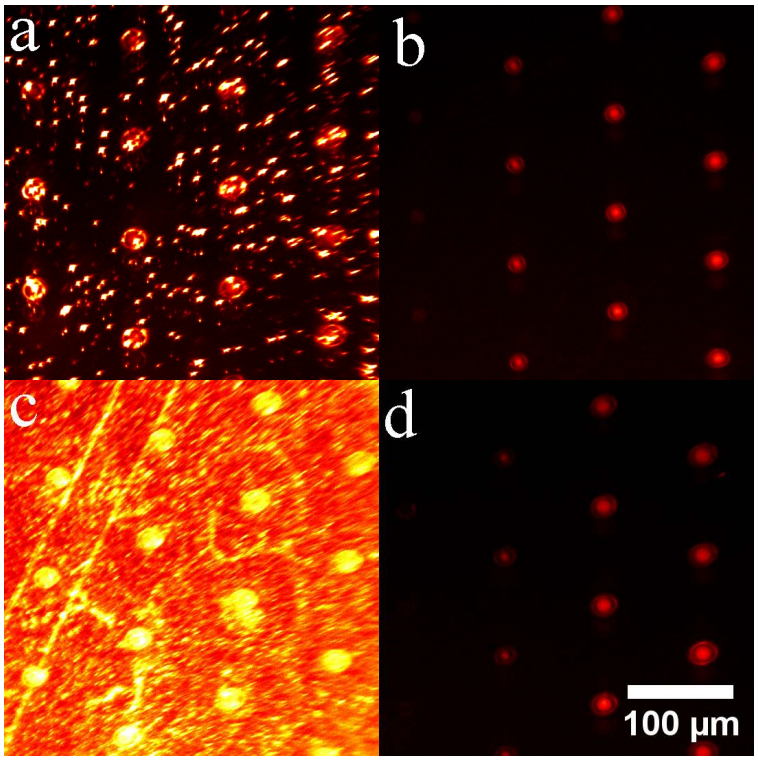

Figure 2: Fluorescence images of coverslips after addition of QDs to the microdisks collected with a 10x objective using a fluorescence microscope with a UV lamp. a and b are microdisks filled respectively with unexchanged QDs and exchanged QDs via the mixing method. c and d are microdisks covered with QDs (unexchanged QDs for c, exchanged QDs for d) via the infusion method. In both (a,c) cases, unexchanged QDs are poorly dispersed, with the formation of clusters and fixation onto the gold surface of the coverslip, while exchanged QDs (b,d cases) are selectively attached to the cavity. Each column on the coverslip is made using the same laser power but a different exposure time, thus leading to different microdisks perimeters for each row, ranging from 25 to 70 µm (see Figure 1c).

After optimizing the fabrication of SU8 microdisk cavities, we then developed a method to insert core/multishell CdSe/CdS/ZnS QDs (Figure S5) inside them homogeneously in their volume, before photolithography, or closer to their surface after photolithography.

After synthesis, the QD surface ligands are oleïc acid and oleylamine, which present long alkyl chains. These molecules enable the dispersion of QDs in apolar solvents but not in cyclopentanone, the SU8 solvent. Therefore, attempts to resuspend QDs in the SU8 solution before spin coating and fabrication of the microdisks resulted in the presence of

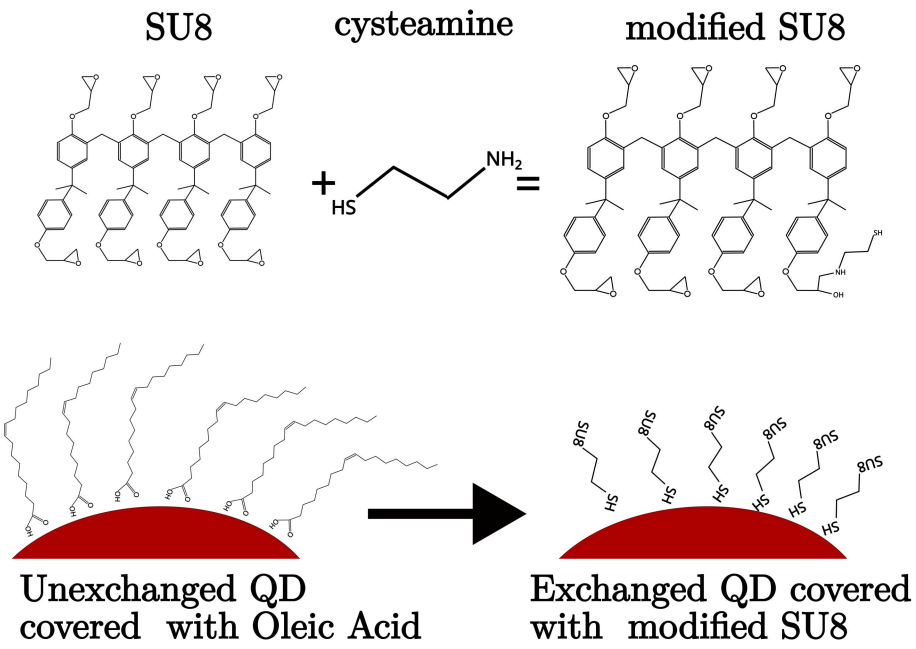

Figure 3: Proposed mechanism for the chemical reaction of ligand creation and exchange. SU8 is mixed with cysteamine in a chloroform solution. The amine group of the cysteamine reacts with an epoxy group of the cysteamine, leading to modified SU8. The thiol group of the modified SU8 can then exchange onto the surface of the Quantum Dots.

large aggregates, which deposited on the microdisks but also on the surface of the coverslip (Figure 2a). Then, we also tested infusion of the QDs near the surface of the microdisks after microfabrication, by first fabricating microdisks in neat SU8 resin, then exposing them to a solution of QDs. A previous study demonstrated homogeneous dispersion of iron oxide nanoparticles when dropped on a photosensitive epoxy resin SU8, when capped with similar alkyl chain ligands[37]. However, with our QDs, this led to massive aggregates when they were deposited in hexane, chloroform and toluene (Figure 2c).

In order to facilitate chemical compatibility between QDs and SU8, two conditions need to be fulfilled: (i) redispersion of QDs in the same solvent as SU8, namely cyclopentanone and (ii) incorporation of the QD within the epoxy network by covalent coupling between the surface ligands and the epoxy groups from SU8, such that the QDs do not become sequestered as aggregates during the epoxy polymerization. Using ligand exchange with mercaptosuccinic acid, Lee et al. demonstrated dispersion of QDs in SU8 at a macroscopic scale, but still with

the presence of aggregates at the microscopic scale[34]. We therefore synthesized a new QD surface ligand by reacting together cysteamine and SU8, so that the amine group react with one of the epoxy moiety on the SU8 and the thiol is available to bind to the QD surface (Figure 3). We select a cysteamine to SU8 ratio of 1:4, such that statistically one SU8 molecule can at most bind to one cysteamine, in order to avoid cross-linking the QDs together via SU8 bound to multiple cysteamines. After this reaction is performed, we introduce QDs in chloroform in order to exchange the native oleic acid/oleylamine ligands with the new cysteamine-SU8 ligands in large excess (typically with a SU8:QD ratio of 40 000:1). After ligand exchange, QDs precipitate in hexane (in contrast to non exchanged QDs which are soluble in hexane). They readily re-disperse in cyclopentanone without agglomeration, as demonstrated by their small hydrodynamic radius ($R_H = 14nm$) measured by dynamic light scattering (Supporting Information Figure S6). FTIR spectroscopy also suggests that the ligand exchange proceeds efficiently (Figure S8). The resulting modified QDs show a good colloidal and optical stability: no significant changes were observed in absorption and emission spectra (apart from a slight $\approx$ 4 nm red shift) or in hydrodynamic diameter one year after ligand exchange and storage in cyclopentanone (see Figures S5 and S6).

The solubility of ligand exchanged QDs in cyclopentanone enables mixing them directly in the SU8-cyclopentanone solution before spin coating and laser exposure. This results in the fabrication of microdisks homogeneously filled with QDs, as shown in Figure 2b. The development step in PGMEA enables removing all of the QDs outside the microdisks, as demonstrated by the absence of any QD fluorescence signal in between microdisks. We also tested the two-step method, first fabricating empty microdisks then incubating them with a solution of ligand exchanged QDs in cyclopentanone. This also results in homogeneous labeling of the microdisks with QDs, as shown in Figure 2d, suggesting that the new SU8-ligands on the QDs are able to react with the remaining epoxy or alcohol functions at the surface of the microdisks. This last method is less consuming in QDs compared to the dispersion of QDs in SU8 before the photolithography. It also deposits QDs preferentially at the surface

of microdisks, not inside. This will favor their coupling with WGM modes, since these are located directly on the side walls of the microdisk surface. We will therefore continue to use this method for the following optical characterization experiments. In both the mixing and infusion methods, the fluorescence intensity of the microdisks does not vary significantly with the microdisk diameter (Figure S17). We realized SEM images of microdisks after infusion with exchanged QDs, and no significant roughness changes was observed, microdisks presented smooth surface after this step (see Figure S4).

2.3 Coupling of QD emission with Whispering Gallery Modes

In this section, we demonstrate the coupling of the QD emission to the WGMs of the microdisks and compare the obtained optical properties with electromagnetic simulations. In the cylindrical geometry, light may undergo total internal reflection at the SU8/air interface above the critical angle. WGMs resonances occur when the electromagnetic field experiences a zero phase shift after having traveled along the interface for a full turn. In this description, resonances are spectrally distant by the free spectral range corresponding to $\Delta\lambda = \frac{\lambda^2}{nL}$ where L is the length of a round trip and n the effective refractive index. In order to characterize these modes in more detail, we realized electromagnetic simulations using finite elements time-domain methods, as described further in the section 4. Figure 4a shows a map of the simulated electromagnetic field of one of the WGM.

Acquisition of QD emission was performed by confocal fluorescence microscopy, with a typical lateral resolution of 1 µm. When acquired in the direction of the vertical axis of the microdisk, the emission spectrum of QDs was identical to the spectrum in solution, without any detectable coupling to WGMs (Figure S9). Indeed, WGM wavevectors lie in the plane perpendicular to the cylinder axis and scattering of WGM at the microdisk surface is expected to occur mainly in the incident wavevector direction[3]. Scattered light from WGMs are thus expected to propagate to the far field in directions tangential to the side walls, perpendicularly to the microdisk axis. In the axial direction, only non-cavity-coupled

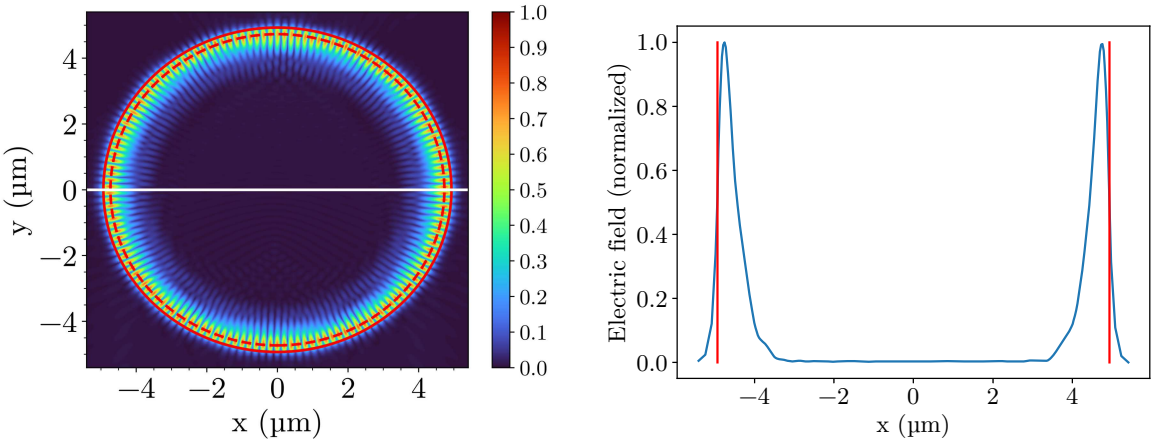

(a) (b)

Figure 4: a) Spatial distribution of absolute electric field amplitude for a resonant whispering mode inside the microdisk. The limit of the microdisk (radius equal to 4.93μm) is represented by the continuous red circle while the dashed red circle represents the position of the maximum of the mode. The wavelength is 603.3 nm . ; b) Field amplitude as a function of the transverse coordinate (along the white line represented on a).

fluorescence could be detected. In order to observe QD fluorescence coupled to WGMs, emission spectra were collected in a direction perpendicular to the axis of the microdisk, by placing the coverslip perpendicular to the axis of the microscope objective (Figure S10). When placing the objective confocal volume on the edges of the microdisks, QD emission spectra indeed showed regularly spaced narrow peaks typical of free spectral range WGMs resonant modes (Figures 5a, b). On the contrary, when the confocal volume was placed on the bottom surface of the side wall, no WGM peaks were detected. This confirms that WGM surface scattering mainly occurs in the plane, in the direction tangential to the side wall (see Figure S11).

The quality factor of WGMs, Q, can be estimated from their spectral widths (full width at half maximum), $\delta\lambda$, as $Q = \frac{\lambda}{\delta\lambda}$, where λ is the central wavelength of the mode. As shown in Figure 5a, the measured spectral width is actually limited by the resolution of the spectrometer, 0.1 nm. This shows that the quality factor of these WGMs can reach values greater than or equal to 6000. For small cavities, the Q factor reaches 6000 for almost all of them, while for the bigger cavities, Q factor decreases to values around 2000. This loss in Q

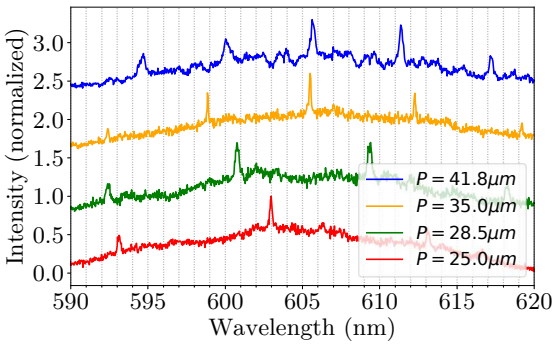

(a)

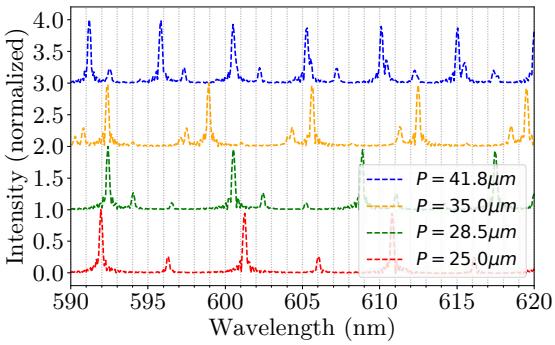

(b)

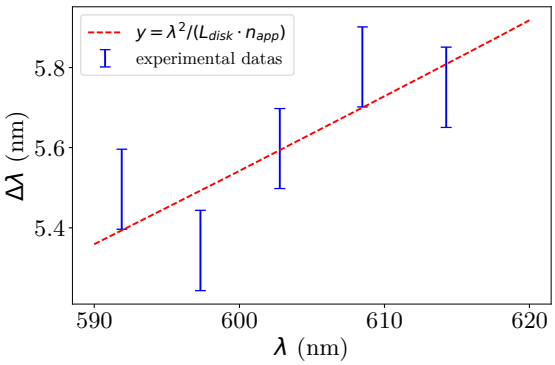

(c)

Figure 5: Experimental intensity spectra (a) and simulated TE field amplitude spectra (b) for different microdisk perimeters. c)Experimental wavelength difference ($\Delta\lambda$) between successive peaks for a cavity perimeter of 41.8μm) as a function of the average wavelength, and fit with equation 3. Error bars of 0.1nm are due to the resolution of the spectrometer. L_{disk} is measured experimentally. The model has only one free parameter which is n_{app}. For this perimeter, our model gives us an experimental $n_{app} = 1.61 \pm 0.1$

factor is assumed to be caused by the diminution of the circularity of the cavity. Indeed, our Q factor is not limited by radiation losses, but mostly by shape and surface roughness. To compare with other polymeric microcavities, Ta et al obtained a Q between 4000 and 8000 using Araldite epoxy resin[14]. Polymeric microfibers made of PMMA reached Q of 6000 to 8200. SU8 hemispheres reached a Q factor of 7030[38]. Our results show that we achieve at least similar Q factor compared to what exists in the literature for the same type of material.

When considering emission spectra of microdisks with different sizes, experimental (Figure 5a) spectra are consistent with simulations (Figure 5b). The absolute wavelengths of observed WGMs deviate from the simulations, due to the experimental uncertainty on the size of the microdisk. Indeed, a 1% experimental uncertainty on the perimeter leads to an error of 6 nm in the predicted wavelength of the mode. However, the error on the spectral distance between modes is only 0.08 nm. Indeed, the experimental and simulated wavelength difference between two successive modes, $\Delta\lambda$, match with a precision of $\approx 5\%$. Using a geometrical optics model, considering that the optical length for a full turn along the microdisk interface corresponds to a multiple integer of the resonant wavelengths, we define an apparent index as $n_{app} = \frac{p\lambda}{L_{disk}}$, where λ is the resonant wavelength, p an integer and L_{disk} is the physical perimeter of the microcavity (Figure 6). In this description, the wavelength difference ($\Delta\lambda$) between successive peaks scales as:

$$\Delta\lambda \approx \frac{\lambda^2}{n_{app} * L_{disk}} \tag{3}$$

The apparent refractive index n_{app} obtained with the simulated spectra, increases with the microdisk size, from ca. 1.5 for smaller microdisks to 1.55 for larger ones. Experimental values of n_{app} are in accordance with the simulations, even though small size disks experience a slightly lower value. This size-dependence may be explained by the localisation of the WGM within the SU8 microdisk and its extension outside as an evanescent wave. As shown from Figure 4b and Figure S14, in the simulations the mode extends as an evanescent

field with a decay length of typically 100-130 nm in air. This leads to an effective refractive index which is slightly smaller than that of SU8. Moreover, the WGM intensity maximum location is not strictly at the interface but inside the disk. For microdisks with radii in the $(1.6 - 6.6)\mu m$ range, simulations show that the distance between the position of the mode intensity maxima and the cavity wall is typically 210 nm (See Figure S13). As we cannot have an experimental measurement of the location of the mode intensity maximum, our definition of the apparent refractive index, n_{app} considers the actual perimeter of the microdisk. Therefore, and by taking into account the fact that the mode is localized mainly in SU8 and partially in air as an evanescent field, the value of n_{app} is very close to the bulk SU8 one, tabulated at $\lambda = 600nm$ to 1.58.

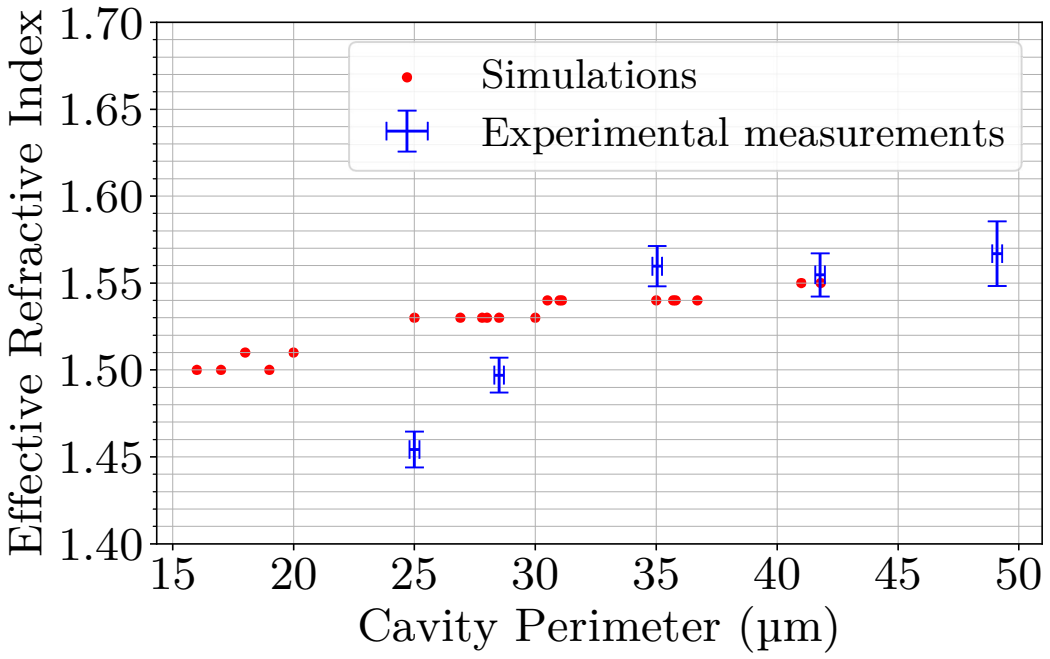

Figure 6: Effective refractive index as a function of the cavity perimeter, for experimental and simulated spectra.

Finally, on some spectra, depending on the position of the pinhole collection, pairs of peaks could be observed (Figure 7a). We performed polarization analysis on the collected fluorescence emission. The resulting spectra show that each of these peaks is polarized

either aligned with the central axis of the cavity or, respectively, perpendicular to it. These peaks can therefore be ascribed to the TE and, respectively, TM modes. The difference in effective refractive index can be calculated using equation 4 where $\delta\lambda_{TETM}$ is the wavelength gap between the TE and TM modes. In the example shown in Figure 7, the experimental difference of refractive index between TE and TM modes is estimated to be about 0.006.

In the simulations, the microdisk of $28.5\mu m$ has a $\delta\lambda_{TETM} = 2.1nm$ at the wavelength $\lambda = 601nm$ and $n_{app} = 1.53$ (see Figure 6). By inserting these values in equation 4 we obtain $\delta n_{app}^{sim} = 0.005$, which is in accordance with the experimental value.

$$\frac{\delta n_{app}}{n_{app}} = \frac{\delta\lambda}{\lambda} \tag{4}$$

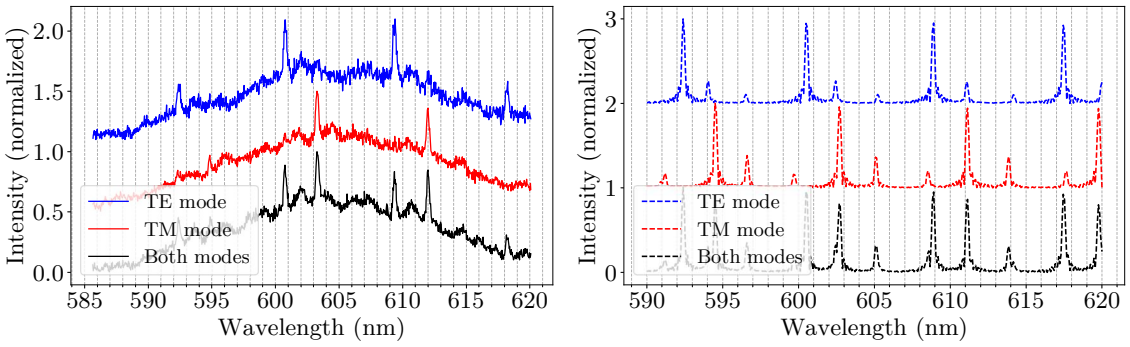

Figure 7: a) Spectra from a 28.5 µm perimeter cavity taken without a polarizer, and with a polarizer either along the microdisk axis (blue curve) or perpendicular to the microdisk axis (red curve). b) Simulated spectra considering either both modes (black curve), only TE mode (red curve) or only TM mode (blue curve). The spectral distance between two adjacent peaks of different modes $\delta\lambda_{TETM}$ gives us the difference of effective refractive index seen by the two modes, using equation 4

2.4 Stability over time

In order to assess the stability of QD emission after ligand exchange and incorporation inside the microdisks (Figure 2 b and d), we compared the fluorescence intensity of the microdisks after one year of storage in air at room temperature. The same images were acquired one year

after the realization of the microdisks (see Figure S17 a and b). The fluorescence intensity of both microdisks preparation remained in the same order of magnitude, which shows the good stability of the QD-loaded microdisks in both cases. When compared relatively to each other, the intensity of the infused microdisks has decreased by roughly 50% compared to the mixed microdisks. This observation suggests that infused QDs are located close to the interface with air. This enables better coupling to WGMs but leads to slightly accelerated aging in the long term. QDs mixed with the resin before microdisk fabrication are better preserved from aging due to their incorporation within the polymeric matrix.

3 Conclusions

We successfully developed a versatile fabrication process of polymeric microcavities by optical lithography 1b. We designed a new ligand to exchange with the native oleic acid ligands surrounding the QDs after synthesis. It enabled the exchanged QDs to be dispersible in SU8 and to naturally bind to the surface of the microdisks, leading to an efficient coupling to the WGMs. Q factors over 6000 were measured, which proves that homogeneous QD incorporation enables preserving high WGM quality factors. The observed spectral features could be modeled accurately by electromagnetic simulations.

These low cost WGM microdisks are good candidates for microlasing, by using high gain nanocrystals such as core shell structures and nanoplatelets as an integrated light source. Gain for such emitters were observed as high as 6000 cm^{-1} under a pulsed laser excitation source.[39] This photolithographic method is simple yet enables a deterministic control over the size and positioning of the disks. This would enable fabrication of regular arrays of microlasers, and precise positioning of microlasers, which offer potential applications in microphotonics and sensing. Quality of the cavity, and optimum positioning of the emitters at the microdisk-edge, will be major advantage for lasing operation. Moreover, the surface of such microdisks can be easily functionalized allowing chemical modifications for specific

interactions. It opens the way for using such surface bound QD microcavities for sensing.

4 Methods

4.1 Materials

SU8-2015 resin was purchased from Kayaku Advanced Materials. All other chemicals were purchased from Sigma-Aldrich and used without further purification.

4.2 Microcavity Fabrication

Describe gold coating. SU8-2015 diluted in cyclopentanone (3:2 in volume) was poured onto the gold-coated coverslip, then spincoated at 1 kRPM for 10 s, followed by 3 kRPM for 1 min, followed by a 10s deceleration. The resin was then soft baked by placing the coverslip on a heating plate at 65°C for 1 min, followed by 2 min at 75°C then left cooling down on the hotplate turned off until reaching 50°C, taking approximately 2 min. The coverslip was then placed on a motorized stage at the focal plane of a microscope objective (typically, 10x, NA 0.3) through which a cw. 405 nm laser (Oxxius) was focused. In order to assure laser cylindrical symmetry, spatial filtering through a single mode fiber (Thorlabs SM300 combined with plan achromatic objectives x20, NA 0.4) is performed. A pattern of microdisks was realized by exposing the resist to the laser for typically 50 ms - 1 s at 500 µW at a fixed position, before moving to the next position. A post exposure bake step was then performed, heating the coverslip for 2 min at 95°C, followed by a development step consisting of immersing the coverslip for 2 min in a stirred bath of propylene glycol monomethyl ether acetate (PGMEA), then rinsing with a bath of isopropanol for 2 minutes. Finally, a hard bake step was applied, heating the sample for 1 min at 120°C, then taking it off the hotplate immediately for a fast cool down, in order to harden the SU8 microdisks as well as smoothing out the surface rugosity.

Two SEM microscopes were used to characterize the microdisks. The first one (Zeiss

Supra 40) requires a gold coating for SU8 dielectric microdisks imaging. For the second one (FEI- Thermofisher Quattro), in the low-vacuum mode, water molecules are sprayed in the room. A thin layer of water is formed onto the surface of the sample, ensuring conductivity and allowing imaging of dielectric materials.

4.3 QD synthesis

CdSe cores were synthesized by reaction of cadmium myristate and selenium powder in octadecene[40]. CdSe core QD size and concentrations were estimated using the absorption wavelength of the first excitonic peak transition and the absorbance at 350 nm[41,42]. Three monolayers of CdS shell, followed by two monolayers of ZnS, were grown using cadmium oleate, zinc oleate and sulfur diluted in octadecene following the SILAR procedure[43].

4.4 QD ligand exchange

10mg of cysteamine were dissolved in 5mL of chloroform. Sonication and strong agitation for 15min were required for dissolution. 720mg of SU8-2015 was added, and this solution was kept in the dark and agitated for 24h. 250µL of CdSeCdSZnS QDs synthesized as described in section 4.3 at a concentration of around 38 µM were precipitated with ethanol and dispersed in 250 µL of chloroform before being added to the solution of cysteamine and SU8. Solution was still kept in the dark and agitated for 24 more hours. The exchanged QDs were then precipitated with hexane and redispersed in 5mL of cyclopentanone.

4.5 QD insertion into microcavities

QDs were used up to one month after ligand exchange to load microdisks. A first method for QD insertion into microcavities consisted in mixing the QD solution, with or without ligand exchange in SU8. To do so, 200 µL of exchanged QDs dispersed were mixed in cyclopentanone at C = 1 µM in 1.8 mL of SU8-2015 diluted as described in 4.2. The QD-

SU8 solution, first stirred for 2 hours, was then used to fabricate microcavities as described in 4.2. The second method used pre-fabricated SU microcavities. 250 µL of a QD solution (with or without ligand exchange) at C = 0,1 µM in cyclopentanone for exchanged QDs and chloroform for unexchanged QDs was deposited on top of the microcavities and let to incubate for 5 min at room temperature. The substrate was then thoroughly rinsed with two baths of cyclopentanone for exchanged QDs (chloroform for unexchanged QDs) and one bath of isopropanol during 10s each with manual stirring.

4.6 Optical characterization

Solution phase absorption and emission spectra were acquired on Cary 5000 spectrometer and an Edinburgh instrument spectrometer. Emission spectrum from QD-loaded microcavities were recorded using an Olympus IX 71 fluorescence microscope, combined with a 100 x (0.8 NA) objective. Excitation was assured with a 405nm continuous laser source (Oxxius LBX-405-50-CSB-PPA), and spectral detection with a Horiba iHR550 spectrometer. Fluorescent images were taken using a 10X objective, a mercury lamp with a (438±12.5nm) excitation filter as an excitation source and a PCO Panda sCMOS camera. Excitation was separated from the detection using a 510nm dichroic filter (Semrock FF510-Di02) plus a 473nm longpass filter (RazorEdge LP Edge Filter 473). To collect the emission propagating in the plane perpendicular to the microdisk axis, the sample was held perpendicular to the objective. A pinhole (diameter = $100\mu m$) located in the microscope image plane ensured collection by a $1\mu m$ size region. Emission spectra were collected from the lateral sides of the microdisks.

4.7 Simulation

4.7.1 Description of the simulated structure

The modes of the microdisks were simulated by finite difference time domain (FDTD) method. The structure simulated is a cylinder with a refractive index $n = 1.59$ corresponding

to the one of the SU8. Since the WGM have a planar circular symmetry, we restricted to 2D simulations, in the (x, y) plane perpendicular to the microdisk z axis. We implement a point-like-dipole as a single light source emitter in order to excite the modes of the system. The dipole is implemented $200nm$ inside the microdisk wall. Its polarisation is set at 45° with the z direction, in the $(x, y \approx 0, z)$ plane. In $(\overrightarrow{u_x}, \overrightarrow{u_y}, \overrightarrow{u_z})$ space, we calculate both the Transverse Electric (TE) mode of the electromagnetic field (H_x, H_y, E_z components) and Transverse Magnetic (TM) mode of the electromagnetic field (E_x, E_y, H_z components). The data are acquired from the 2D simulation plane, on a square whose limit is set $500nm$ away from microdisk wall.

The emission spectrum of the dipole has a Gaussian shape with a bandwidth of $590 - 620nm$, corresponding to a pulsed excitation of $50fs$. We let the system evolving freely over $6000fs$ ensuring a $0.2 - 0.4nm$ spectral resolution. We use a mesh of 9nm in the material. Finally, the simulation region is a square extending 1µm away from the cylinder. Outside the microdisk the boundary conditions were set as fully absorption layers which do not allow the light to get reflected back. In this way we simulate an open environment where the uncoupled part of the light propagates to infinity.

4.7.2 Field amplitude

The field amplitude is calculated by the following equation

$$E = \sqrt{E_x^2 + E_y^2 + E_z^2} \tag{5}$$

Absolute value of the Electromagnetic field amplitude of one resonant WGM is represented in Figure 4a. On the ring we can observe 122 maxima and minima. This corresponds to an order of interference p ($p\lambda = L$) equal to 61.

We calculate E_{int}, proportional to the total electric field amplitude inside the cavity, by

integrating the absolute value of the electromagnetic field amplitude along a circular line profile positioned $200nm$ inside the cylinder wall (position of the maximas, represented by a dashed red circle on Figure 4a) with a width of 10 pixels. We do that for the different electromagnetic map we obtained for each wavelength to obtain a simulated spectrum.

In order to represent the radial variation of the WGM Electromagnetic field amplitude, we calculate the average of the electric field amplitude on a straight line profile of 10 pixels width (Figure 4). We estimate the extension of the evanescent part of the mode outside the disk by realizing an exponential fit with a characteristic decay length. In the supplementary information, we plot the decay length of the evanescent field with respect for different microdisk radiuses for the first mode in the spectral range considered ($\lambda > 590nm$ (Figure S14).

In order to represent the electromagnetic field spectrum, we calculate E_{int}, proportional to the total electric field amplitude inside the cavity, by integrating the absolute value of the electromagnetic field amplitude along a circular line profile positioned 200nm inside the cylinder wall with a width of 10 pixels (continuous red line on figure 4a).

The same spectral analysis has been performed for different disk perimeters corresponding to experimental ones: 25µm, 28.5µm, 35.04µm, 41.78µm and 49.1µm. All the spectra exhibit resonant modes. For each diameter, experimental and theoretical wavelength gap ($\Delta\lambda$) are equal with a precision of $0.2 - 0.4nm$.

Funding

Financial support for this project was provided by the Institute of Materials Science (iMAT) of the Alliance Sorbonne Université. CK acknowledges iMAT for a PhD grant. The authors acknowledge funding from the Agence Nationale pour la Recherche (Nanowhispers, ANR-21-CE42-0029).

Acknowledgement

We acknowledge Xiangzhen XU for TEM imaging.

Supporting Information Available

Additional experimental protocols and characterization.

References

(1) Chiasera, A.; Dumeige, Y.; Féron, P.; Ferrari, M.; Jestin, Y.; Nunzi Conti, G.; Pelli, S.; Soria, S.; Righini, G. Spherical whispering-gallery-mode microresonators: Spherical WGM microresonators. Laser & Photonics Reviews **2010**, 4, 457–482.

(2) Matsko, A. B.; Ilchenko, V. S. Optical Resonators With Whispering-Gallery Modes—Part I: Basics. IEEE JOURNAL OF SELECTED TOPICS IN QUANTUM ELECTRONICS **2006**, 12, 12.

(3) Yang, S.; Wang, Y.; Sun, H. Advances and Prospects for Whispering Gallery Mode Microcavities. Advanced Optical Materials **2015**, 3, 1136–1162.

(4) Toropov, N.; Cabello, G.; Serrano, M. P.; Gutha, R. R.; Rafti, M.; Vollmer, F. Review of biosensing with whispering-gallery mode lasers. Light: Science & Applications **2021**, 10, 42.

(5) Jana, S.; Xu, X.; Klymchenko, A.; Reisch, A.; Pons, T. Microcavity-Enhanced Fluorescence Energy Transfer from Quantum Dot Excited Whispering Gallery Modes to Acceptor Dye Nanoparticles. ACS Nano **2021**, 15, 1445–1453.

(6) Ouyang, X.; Liu, T.; Zhang, Y.; He, J.; He, Z.; Zhang, A. P.; Tam, H.-Y. Ultrasen-

sitive optofluidic enzyme-linked immunosorbent assay by on-chip integrated polymer whispering-gallery-mode microlaser sensors. Lab on a Chip **2020**, 20, 2438–2446.

(7) Vollmer, F.; Arnold, S. Whispering-gallery-mode biosensing: label-free detection down to single molecules. Nature Methods **2008**, 5, 591–596.

(8) Pöllinger, M.; O'Shea, D.; Warken, F.; Rauschenbeutel, A. Ultrahigh- Q Tunable Whispering-Gallery-Mode Microresonator. Physical Review Letters **2009**, 103, 053901.

(9) Shi, L.; Zhu, T.; Huang, D.; Liu, M.; Deng, M.; Huang, W. In-fiber whispering-gallery-mode resonator fabricated by femtosecond laser micromachining. Optics Letters **2015**, 40, 3770.

(10) Tessarek, C.; Sarau, G.; Kiometzis, M.; Christiansen, S. High quality factor whispering gallery modes from self-assembled hexagonal GaN rods grown by metal-organic vapor phase epitaxy. Optics Express **2013**, 21, 2733.

(11) Chen, R.; Ling, B.; Sun, X. W.; Sun, H. D. Room Temperature Excitonic Whispering Gallery Mode Lasing from High-Quality Hexagonal ZnO Microdisks. Advanced Materials **2011**, 23, 2199–2204.

(12) Hossein-Zadeh, M.; Vahala, K. J. Free ultra-high-Q microtoroid: a tool for designing photonic devices. Optics Express **2007**, 15, 166.

(13) Grimaldi, I. A.; Berneschi, S.; Testa, G.; Baldini, F.; Nunzi Conti, G.; Bernini, R. Whispering gallery modes in self-assembled bottle microresonators coupled to planar waveguide. SPIE OPTO. San Francisco, California, United States, 2016; p 97501H.

(14) Ta, V. D.; Chen, R.; Sun, H. D. Self-Assembled Flexible Microlasers. Advanced Materials **2012**, 24, OP60–OP64.

(15) Duong Ta, V.; Chen, R.; Ma, L.; Jun Ying, Y.; Dong Sun, H. Whispering gallery mode

microlasers and refractive index sensing based on single polymer fiber: Microlasers and refractive index sensing. Laser & Photonics Reviews **2013**, 7, 133–139.

(16) Tang, S. K. Y.; Derda, R.; Quan, Q.; Lončar, M.; Whitesides, G. M. Continuously tunable microdroplet-laser in a microfluidic channel. Optics Express **2011**, 19, 2204.

(17) Haase, J.; Shinohara, S.; Mundra, P.; Risse, G.; Lyssenko, V. G.; Fröb, H.; Hentschel, M.; Eychmüller, A.; Leo, K. Hemispherical resonators with embedded nanocrystal quantum rod emitters. Applied Physics Letters **2010**, 97, 211101.

(18) Wang, Y.; Ta, V. D.; Leck, K. S.; Tan, B. H. I.; Wang, Z.; He, T.; Ohl, C.-D.; Demir, H. V.; Sun, H. Robust Whispering-Gallery-Mode Microbubble Lasers from Colloidal Quantum Dots. Nano Letters **2017**, 17, 2640–2646.

(19) Ta, V. D.; Yang, S.; Wang, Y.; Gao, Y.; He, T.; Chen, R.; Demir, H. V.; Sun, H. Multicolor lasing prints. Applied Physics Letters **2015**, 107, 221103.

(20) Wang, Y.; Fong, K. E.; Yang, S.; Ta, V.; Gao, Y.; Wang, Z.; Nalla, V.; Demir, H. V.; Sun, H. Unraveling the ultralow threshold stimulated emission from CdZnS/ZnS quantum dot and enabling high-Q microlasers. Laser & Photonics Reviews **2015**, 9, 507–516.

(21) Zhao, J.; Yan, Y.; Gao, Z.; Du, Y.; Dong, H.; Yao, J.; Zhao, Y. S. Full-color laser displays based on organic printed microlaser arrays. Nature Communications **2019**, 10, 870.

(22) Gong, X.; Qiao, Z.; Guan, P.; Feng, S.; Yuan, Z.; Huang, C.; Chang, G.-E.; Chen, Y.-C. Hydrogel Microlasers for Versatile Biomolecular Analysis Based on a Lasing Microarray. Advanced Photonics Research **2020**, 1, 2000041.

(23) Yuyama, K.-i.; Kawaguchi, H.; Wei, R.; Omatsu, T. Fabrication of an Array of Hemispherical Microlasers Using Optical Vortex Laser-Induced Forward Transfer. ACS Photonics **2023**, 10, 4045–4051.

(24) Cai, L.; Pan, J.; Hu, S. Overview of the coupling methods used in whispering gallery mode resonator systems for sensing. Optics and Lasers in Engineering **2020**, 127, 105968.

(25) García de Arquer, F. P.; Talapin, D. V.; Klimov, V. I.; Arakawa, Y.; Bayer, M.; Sargent, E. H. Semiconductor quantum dots: Technological progress and future challenges. Science **2021**, 373, eaaz8541.

(26) Anbumani, S.; da Silva, A. M.; Roggero, U. F.; Silva, A. M.; Hernández-Figueroa, H. E.; Cotta, M. A. Oxygen plasma-enhanced covalent biomolecule immobilization on SU-8 thin films: A stable and homogenous surface biofunctionalization strategy. Applied Surface Science **2021**, 553, 149502.

(27) Nagaiyanallur, V. V.; Kumar, D.; Rossi, A.; Zürcher, S.; Spencer, N. D. Tailoring SU-8 Surfaces: Covalent Attachment of Polymers by Means of Nitrene Insertion. Langmuir **2014**, 30, 10107–10111.

(28) Xin, Y.; Pandraud, G.; Otten, L.; Zhang, Y.; French, P. Surface Functionalization of SU-8 Vertical Waveguide for Biomedical Sensing: Bacteria Diagnosis. EUROSENSORS 2018. 2018; p 1081.

(29) Cao, C.; Birtwell, S.; Høgberg, J.; Morgan, H.; Wolff, A.; Bang, D. Gold Nanoparticles-Coated SU-8 for Sensitive Fluorescence-Based Detections of DNA. Diagnostics **2012**, 2, 72–82.

(30) Beckwith, K. S.; Cooil, S. P.; Wells, J. W.; Sikorski, P. Tunable high aspect ratio polymer nanostructures for cell interfaces. Nanoscale **2015**, 7, 8438–8450.

(31) Ehlert, S.; Taheri, S. M.; Pirner, D.; Drechsler, M.; Schmidt, H.-W.; Förster, S. Polymer Ligand Exchange to Control Stabilization and Compatibilization of Nanocrystals. ACS Nano **2014**, 8, 6114–6122.

(32) Hahm, D.; Park, J.; Jeong, I.; Rhee, S.; Lee, T.; Lee, C.; Chung, S.; Bae, W. K.; Lee, S. Surface Engineered Colloidal Quantum Dots for Complete Green Process. ACS Applied Materials & Interfaces **2020**, 12, 10563–10570.

(33) Zou, W.; Du, Z.-j.; Li, H.-q.; Zhang, C. A transparent and luminescent epoxy nanocomposite containing CdSe QDs with amido group-functionalized ligands. Journal of Materials Chemistry **2011**, 21, 13276.

(34) Lee, S. Designing of low-cost, eco-friendly, and versatile photosensitive composites / inks based on carboxyl-terminated quantum dots and reactive prepolymers in a mixed solvent: Suppression of the coffee-ring strain and aggregation. Polymer **2019**, 182, 121839.

(35) Barhum, H.; Kolchanov, D. S.; Attrash, M.; Unis, R.; Alnis, J.; Salgals, T.; Yehia, I.; Ginzburg, P. Thin-film conformal fluorescent SU8-phenylenediamine. Nanoscale **2023**, 15, 17544–17554.

(36) Nguyen, D. T. T.; Tong, Q. C.; Ledoux-Rak, I.; Lai, N. D. One-step fabrication of submicrostructures by low one-photon absorption direct laser writing technique with local thermal effect. Journal of Applied Physics **2016**, 119, 013101.

(37) Ingrosso, C.; Sardella, E.; Keller, S.; Dohn, S.; Striccoli, M.; Agostiano, A.; Boisen, A.; Curri, M. L. Surface Functionalization of Epoxy-Resist- Based Microcantilevers with Iron Oxide Nanocrystals. Advanced Materials **2010**, 22, 3288–3292.

(38) Zhang, Z.; Yao, N.; Pan, J.; Zhang, L.; Fang, W.; Tong, L. A new route for fabricating polymer optical microcavities. Nanoscale **2019**, 11, 5203–5208.

(39) Guzelturk, B.; Pelton, M.; Olutas, M.; Demir, H. V. Giant Modal Gain Coefficients in Colloidal II–VI Nanoplatelets. Nano Letters **2019**, 19, 277–282.

(40) Yang, Y. A.; Wu, H.; Williams, K. R.; Cao, Y. C. Synthesis of CdSe and CdTe Nanocrystals without Precursor Injection. Angewandte Chemie International Edition **2005**, 44, 6712–6715.

(41) Leatherdale, C. A.; Woo, W.-K.; Mikulec, F. V.; Bawendi, M. G. On the Absorption Cross Section of CdSe Nanocrystal Quantum Dots. The Journal of Physical Chemistry B **2002**, 106, 7619–7622.

(42) Yu, W. W.; Qu, L.; Guo, W.; Peng, X. Experimental Determination of the Extinction Coefficient of CdTe, CdSe, and CdS Nanocrystals. Chemistry of Materials **2003**, 15, 2854–2860.

(43) Li, J. J.; Wang, Y. A.; Guo, W.; Keay, J. C.; Mishima, T. D.; Johnson, M. B.; Peng, X. Large-Scale Synthesis of Nearly Monodisperse CdSe/CdS Core/Shell Nanocrystals Using Air-Stable Reagents via Successive Ion Layer Adsorption and Reaction. Journal of the American Chemical Society **2003**, 125, 12567–12575.

TOC Graphic

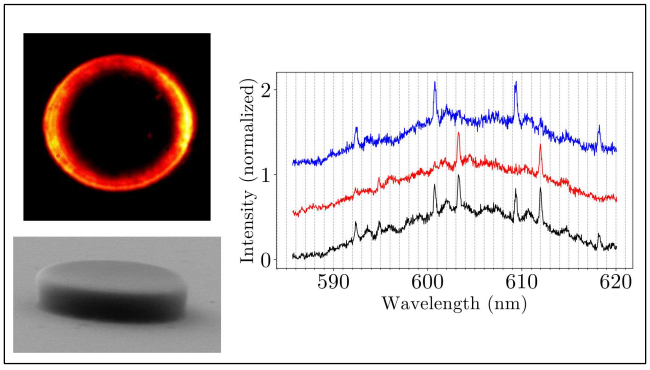

On the left are presented a fluorescence and a SEM image of a microdisk, while a spectrum is represented on the left.